Observations of Temperature Microstructure in NATRE

JEFFREY T. SHERMAN AND RUSS E. DAVIS

Scripps Institution of Oceanography, La Jolla, California

(Manuscript received 7 February 1994, in final form 13 September 1994)

ABSTRACT

A new autonomous instrument collected 76 profiles of temperature microstructure over a ten-day period in the eastern subtropical North Atlantic as part of the North Atlantic Tracer Release Experiment. The data between 200-m and 350-m depth was used to determine the mean rate of temperature variance dissipation $\langle \chi \rangle$. The estimated diapycnal diffusivity is $K_V = 1.4 \times 10^{-5}$ m^2 s^{-1}. The distribution of χ is approximately lognormal, suggesting that the 95% confidence limits on $\langle \chi \rangle$ are ±4%. This uncertainty is less than that caused by the imperfectly known probe response, possible noise spikes on the probes, and variability in the degree of microstructure anisotropy; the latter two effects were estimated from a pair of closely spaced probes. Each of these uncertainties is about ±15%. Statistically significant low-frequency variability of χ is observed with $\langle \chi \rangle$ decreasing by a factor of 2 between the first and second half of the observation. This low-frequency variability is likely the largest cause of error in estimating a seasonally averaged diapycnal diffusivity.

1. Introduction

There is a long standing discrepancy between the values of the diapycnal eddy diffusivity K_V inferred from microstructure observations using the Osborn–Cox model and the diffusivities inferred from model fits to large-scale property distributions (Davis 1994a). Munk (1966) estimated K_V from the vertical advection–diffusion equation $w\partial C/\partial z = K_V \partial^2 C/\partial z^2$. Using an average density profile for depths of 1 to 4 km and an estimated vertical velocity w he found $K_V = O(10^{-4}$ m^2 s$^{-1})$. Today's basin-scale models either use similarly large diapycnal diffusivities (perhaps by failing to separate vertical and diapycnal fluxes) or produce weak over-turning circulations. Osborn and Cox (1972) showed that a simplified temperature variance budget led to a balance of dissipation and production by diapycnal fluxes in which

$$K_V = \frac{\langle \chi \rangle}{2 \langle \partial\theta/\partial z \rangle^2}, \qquad (1)$$

where $\langle \chi \rangle$ is the mean rate of temperature variance dissipation. Since the pioneering efforts to develop oceanographic instruments to measure χ, the K_Vs obtained from (1) have been O (10) times smaller than Munk's value. Although more elaborate advection–diffusion models have been used to examine basin-scale property distributions and more extensive and better measured microstructure datasets have been used with (1), the gap between values of K_V has persisted (Gregg 1987; Davis 1994a).

It is possible that the K_V discrepancy results from some fundamental error in large-scale models, in the Osborn–Cox model's simplifications, or in the idea that K_V measured in midocean thermoclines should be directly compared with the parameters in the large-scale models. Magnified mixing near boundaries (Garrett 1991), increased mixing at great depth (Gargett and Holloway 1984), time variations and lateral mixing (Davis 1994a), the effects of the nonlinear equation of state for seawater (McDougall and You 1990), and the scaling simplifications in the Osborn–Cox model (Davis 1994b) have all been implicated in trying to resolve the discrepancy. Alternatively, Baker and Gibson (1987) have suggested that if χ were adequately sampled so that the long-term average $\langle \chi \rangle$ could be accurately determined, then the measured K_V would be O(10^{-4}m^2 s^{-1}).

The Baker and Gibson argument is based on the high intermittency of χ and the high skewness of its approximately lognormal probability distribution. As a consequence, an unbiased estimator of the mean value is much more likely to underestimate the mean than to overestimate it. Because of the expense and difficulty of attending instruments at sea over a wide range of conditions, microstructure datasets are generally of short duration (~1 month maximum) and this makes it possible that the infrequent large events responsible for a K_V of O(10^{-4} m^2 s^{-1}) have not been adequately sampled. The Long-Term Autonomous Microstructure Profiler (LAMP) is an instrument designed to address this problem by collecting many profiles, of O(100), autonomously over deployments of

Corresponding author address: Dr. Jeffrey T. Sherman, Scripps Institution of Oceanography, La Jolla, CA 92093-0230.
E-mail: jsherman@nemo.ucsd.edu

several months duration. LAMP consists of an autonomously profiling ALACE float (Davis et al. 1992) outfitted with two microtemperature probes and a 200-Mbyte hard disk for data recording (see Fig. 1). In May 1992, the prototype LAMP was deployed in the eastern subtropical North Atlantic in the area of the North Atlantic Tracer Release Experiment for a ten-day period as a trial.

The purpose of this paper is to describe the LAMP (section 2) and the May 1992 dataset (section 3). The sources of errors in estimating $\langle \chi \rangle$ and the statistics of χ are examined in sections 4 and 5. In section 6 the degree of microstructure isotropy is examined using the two probes and leads to a corrected value of $\langle \chi \rangle$, about 30% lower than if all events were isotropic. Spectra over 0.5-m segments were normalized in amplitude and wavenumber and then averaged for comparison to the Batchelor spectrum in section 7. Many individual spectra do not, of course, fit the Batchelor prediction, but the average spectrum has this form.

2. The long-term autonomous microstructure profiler

The LAMP is based on the Autonomous Lagrangian Circulation Explorer (ALACE) described by Davis et al. (1992). The ALACE is a Swallow float intended to track ocean currents to a depth of 2 km. Instrument buoyancy is periodically increased by pumping oil into an external bladder, causing ALACE to rise to the surface where it is located by, and relays data to, the Argos satellite system. The instrument's ability for vertical cycling has been exploited to routinely collect, and relay though Argos, profiles of ocean temperature and salinity in profiling ALACEs. Dozens of temperature profiling PALACEs are in service and CTD profilers are in advanced development. The LAMP differs fundamentally from these instruments. Due to the high data rate required for microstructure measurements, the LAMP internally records during all of its cycles. After a prescribed number of profiles, LAMP remains on the surface transmitting to Argos. Using the Argos locations (~1 km accuracy) for initial guidance and a shipboard direction finder tuned to the Argos frequency for final guidance, the instrument is recovered.

Microstructure measurements are made by two microtemperature probes and recorded on a 200-Mbyte hard disk (Fig. 1). A pair of probes, separated horizontally 18 cm, provides a cross-check on sensor health and minimal sampling of the horizontal scales of microstructure. It also increases the odds of having at least one probe survive a long deployment. Data is recorded while the instrument is descending. Normal descent rate during data acquisition is 5–8 cm s^{-1}. The temperature probes and front-end electronics are manufactured by Sea-Bird Electronics (SBE). The temperature probes are fast response thermistors (FP07). Their output is high-pass filtered on the SBE analog board and sampled by a 16-bit digitizer con-

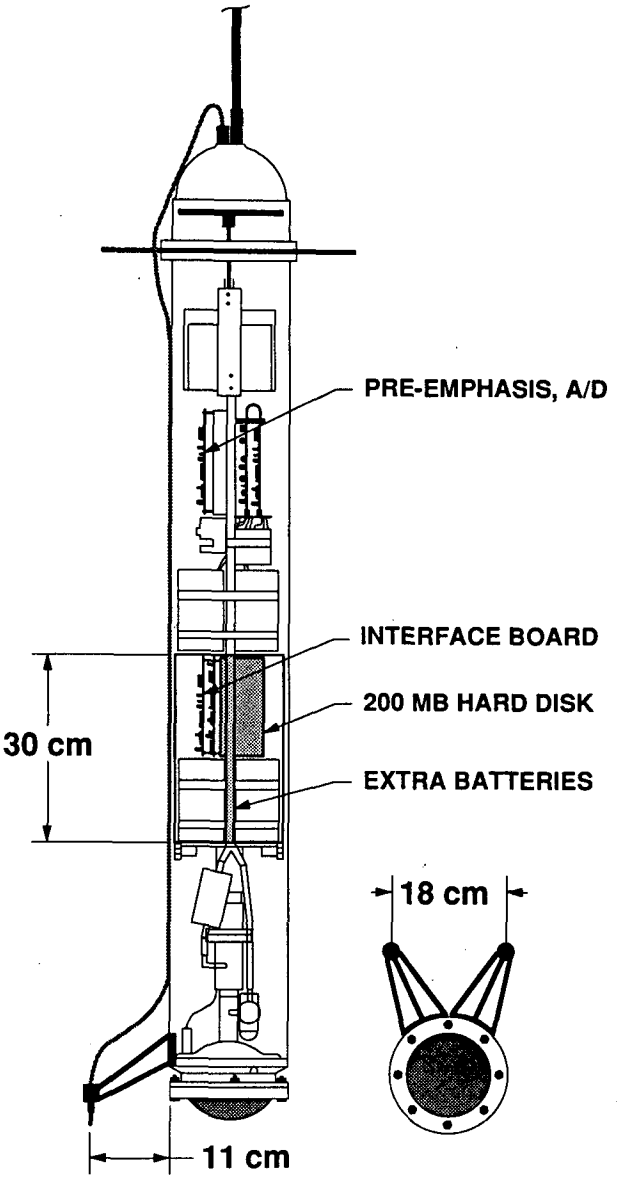

FIG. 1. The LAMP is a 30-cm stretched version of a normal ALACE. Extra room accommodates the 200-Mb hard disk plus extra batteries required. The microtemperature probes are located near the bottom end cap, horizontally separated by 18 cm.

trolled by an Onset TattleTale 6 microcomputer. At the end of each profile the data is written to hard disk. Power is supplied by three parallel lithium 30-amp-hour, 15-volt battery packs (compared to two packs for a standard ALACE). To accommodate the added electronics and batteries, the standard ALACE pressure case has been extended 0.3 m to a total length of 1.24 m and to a mass of 30 kg.

In case a malfunction causes low battery voltage, the instrument goes into a low-power state for the remainder of the scheduled deployment and then switches on a spare battery pack for final pumping to the bladder

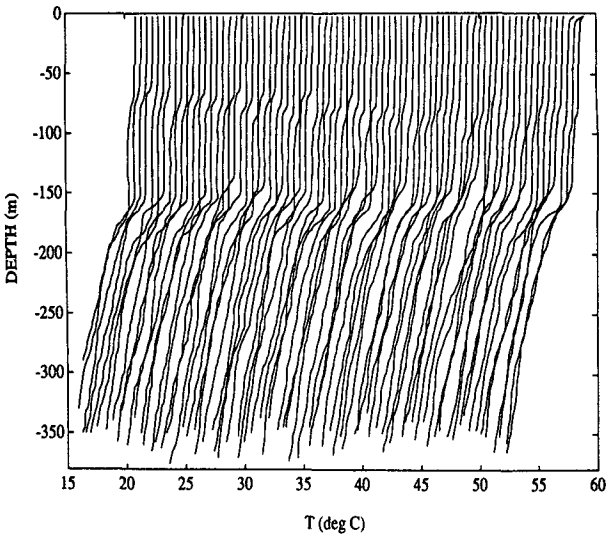

FIG. 2. Cascade plot of 76 temperature profiles shows a remnant mixed layer between 75 and 150 m depth. Profiles are taken every 3 h and are offset by 0.5°C.

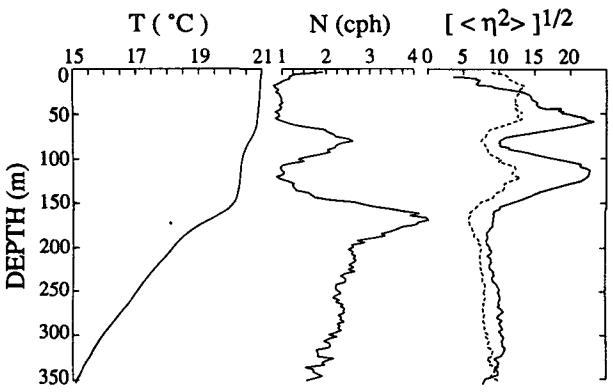

FIG. 3. From the mean temperature profile (left solid line), the corresponding Väisälä frequency profile N is calculated (middle solid line). Measured rms vertical displacement η (right solid line) is compared with the Garrett and Munk internal wave model (dashed line). Their model has ~50% less variance than the measured values for $z > 200$ m.

and Argos transmission. The spare battery provides power for 90 days of Argos transmission at the end of deployment.

3. The May 1992 dataset

In May 1992, the first leg of the North Atlantic Tracer Release Experiment (NATRE) was conducted near 26°N, 28°W. NATRE is a multi-investigator effort to directly measure diapycnal eddy mixing by tracking the vertical spread of intentionally released SF_6. The vertical profile of tracer concentration was measured within a month of its initial release and at approximately 6 and 12 months after release (Ledwell et al. 1993). While the SF_6 was being released along an isopycnal near 300-m depth, LAMP was deployed for a ten-day period to collect 76 profiles (one every 3 hours) to an average depth of 350 m. Average horizontal drift rate was 4 cm s^{-1}, with LAMP finishing 40 km away from its deployment site. The time series of temperature profiles in Fig. 2 shows a remnant mixed layer between 75 and 150 m, followed by the seasonal thermocline. The deployment-average profiles of temperature T and buoyancy frequency N (Fig. 3) exhibit a fairly constant temperature gradient below 200 m. Density was computed using the T–S relationship measured by Schmitt (1992) on a cruise conducted just prior to the NATRE leg.

Potential temperature profiles were computed and isotherms tracked. The isotherm displacement η has rms values of 10 m below 200 m (Fig. 3). High rms η above 150 m results when changes in the mean mixed-layer temperature cause isotherms to migrate across the mixed layer. In comparison, the Garrett–Munk (GM) internal wave model (i.e., Munk 1981) predicts rms $\eta = (3 \text{ cph}/N)^{1/2}$ 7 m; Fig. 3 shows the predicted values for the measured N profile. The observed values show about 50% more variance than the GM model for $z > 200$ m. Agreement between GM and measured rms η near 350-m depth is an artifact of the measuring process. Only a few profiles go to this depth, causing the rms displacements to be biased toward zero. Although a 10-day record provides marginal resolution of tidal frequencies, the spectrum does show a distinct peak at 2 cpd (Fig. 4).

Investigation of the thermal dissipation rate χ concentrated below 200 m, where $\partial T/\partial z$ is fairly constant and statistics of χ are most representative of the dissipation rate near the tracer at 300 m. Time series of χ (computed from $\partial T/\partial z$ assuming isotropy) display intermittency, with only a few high-intensity events (Fig. 5). One such event occurs near 215 m in profile 18, where, although there is no overturning in T on 0.5-m scales, there are high χ values extending over a

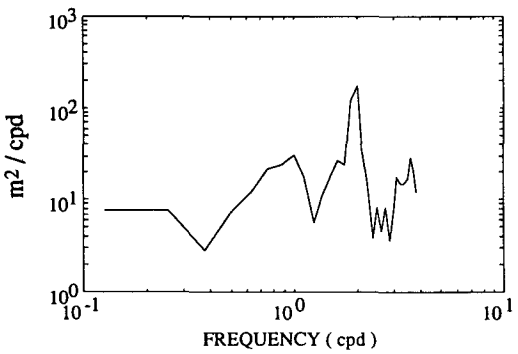

FIG. 4. Frequency spectrum of η shows a tidal peak at 2 cpd. The 10-day record does not allow very good frequency resolution. Profiles are separated by 3 h, such that high-frequency variance is aliased into lower-frequency spectral estimates.

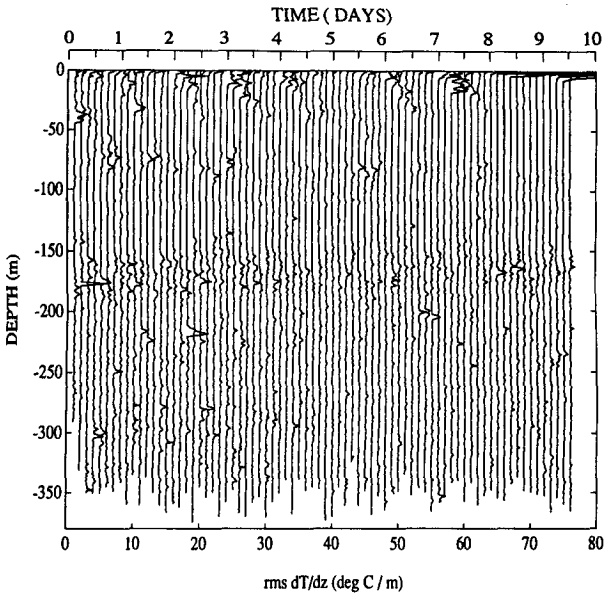

FIG. 5. Rms dT/dz values for all 76 profiles display the high degree of intermittency of large χ events. Larger values near 180 m mark the start of the seasonal thermocline. Profiles are offset by 1°C m^{-1}, so the x axis also represents the profile number.

7-m range (Fig. 6). The χ in this one event accounts for 10% of the time- and depth-integrated χ measured below 200 m and doubles deployment-averaged $\langle \chi \rangle$ in the range of 215–220 m. This dependency of $\langle \chi \rangle$ on a few events, typical of all ocean datasets, is what makes it so difficult to determine the mean dissipation and is responsible for the skewed distribution that, as Baker and Gibson (1987) point out, makes it likely that $\langle \chi \rangle$ is underestimated when χ is undersampled.

4. Estimating $\langle \chi \rangle$

Let the temperature be the ensemble-mean $\langle T \rangle$ plus a fluctuating component: $T = T' + \langle T \rangle$. The thermal dissipation rate is

$$\chi = 2\kappa[(T'_x)^2 + (T'_y)^2 + (T'_z)^2] \equiv 2\kappa I(T'_z)^2, \quad (2)$$

where κ is the molecular thermal diffusivity and subscripts refer to components of the gradient. Typically, T is measured along vertical profiles, resolving only $T_z = T'_z + \langle T_z \rangle$. Statistics of χ must then be estimated by assuming a relation between statistics of $|\nabla T'|^2$ and $(T'_z)^2$ (i.e., $I = 3$ for isotropic flow or $I = 1$ for complete stratification). Inferred statistics of χ will depend on the value of I, which is itself time dependent, and the technique used to estimate $\langle T_z \rangle$. Like previous investigators, we assume a constant value of $I = 3$; this is discussed further in section 6.

The effect of errors in estimating $\langle T_z \rangle$ is investigated by exploring four methods of estimating the mean gradient. Since χ is usually averaged over some depth range Δz, $\langle T_z \rangle$ is often taken as $\overline{T}_z$, the spatial average over Δz. This exaggerates the ensemble mean $\langle T_z \rangle$ if variability on the scale Δz and larger is significant. The dissipation based on this mean gradient estimate will be referred to as χ_0.

As discussed by Davis (1994b), if the Osborn–Cox model is to describe the fluxes that establish the general circulation, the average $\langle \cdot \rangle$ should extend over multiyear timescales and over all seasons. This is necessary to remove the effects of straining by internal waves and mesoscale activity that causes $\overline{T}_z$ to differ from the long-term mean gradient associated with the general circulation. As an approximation of this long-time average, $\langle T_z \rangle$ has been estimated by averaging over all 76 profiles and fitting this profile to a smooth curve. This estimate is called χ_1.

Another method, advocated by Dillon (1982), is to compute the Thorpe temperature profile (resorting the profile to remove all overturns) and use the Thorpe gradient, denoted G_T for the mean gradient. In a very active region, where the local mean gradient $\overline{T}_z$ may equal zero, G_T may yield a better estimate of the background gradient. Since the maximum and minimum values of T for each Δz segment defines $G_T = (T_{\max} - T_{\min})/\Delta z$, the Thorpe gradient is always greater than or equal to $\overline{T}_z$ and, consequently, $\langle G_T \rangle$ is a biased estimator of $\langle T_z \rangle$ (Table 1 indicates it overestimates $\langle T_z \rangle$ by 20%). Values of χ based on G_T will be referred to as χ_2.

The final technique is not to remove a mean value (i.e., $\langle T_z \rangle = 0$). Where the local variance is much greater than the mean, the value chosen for $\langle T_z \rangle$ will make little difference. However, where the local variance is very small, χ can be dominated by $\langle T_z \rangle$. Although taking the mean gradient to vanish does not significantly affect $\langle \chi \rangle$, it does alter its probability density function (pdf) at small χ. The dissipation estimated by this approach is called χ_3.

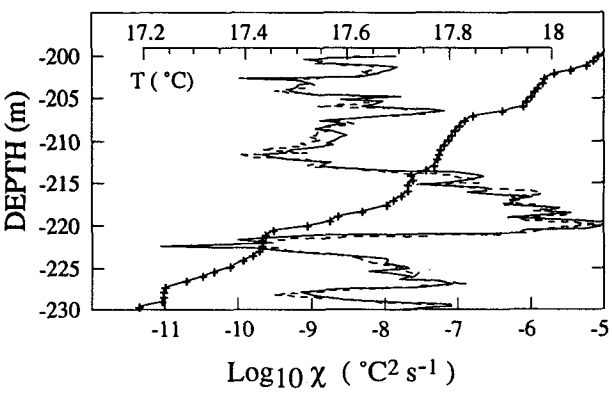

FIG. 6. An expanded section from 200 to 230 m depth of profile 18 shows no temperature inversions on 0.5-m scales (solid line marked with +, scales with upper axis). Measurements of χ (solid line: probe 1, dashed line: probe 2) delineates an active patch from 213 to 220 m.

TABLE 1. Values of $\langle \chi \rangle$ computed using different estimates of the mean gradient. Averages are based on 23 000 nonoverlapping 0.5-m averages for $z > 200$ m. Values of $\sigma^2_{\ln\chi}$ are derived by fitting the pdf to a lognormal distribution to minimize the χ^2 measure of misfit (see text). The deployment-average value of $\langle T_z \rangle$ is given for each estimator, the Thorpe gradient is biased high. $\langle \chi_0 \rangle$ is smaller than the other estimates because the local "mean" gradient includes some of the gradient variability. The mean dissipation computed from the lognormal fit, $\langle \tilde{\chi} \rangle$, is somewhat smaller than the mean obtained by straight averaging, even though it would be biased above the true mean if χ were truly lognormal.

Estimator	$\langle \chi \rangle \times 10^8$ ($K^2\ s^{-1}$)	$\sigma^2_{\ln\chi}$	$\langle T_z \rangle$ ($K\ m^{-1}$)	$\langle \chi_i \rangle / \langle \chi_0 \rangle$	$\langle \tilde{\chi}_i \rangle / \langle \chi_i \rangle$
χ_0 (local)	1.21	3.56	0.020	1.0	0.88
χ_1 (seasonal)	1.25	3.75	0.020	1.03	0.82
χ_2 (Thorpe)	1.22	3.57	0.024	1.01	0.91
χ_3 (zero mean)	1.28	3.53	0.0	1.06	0.88

Here χ was calculated over 0.5-m intervals with a 0.25-m overlap between sequential estimates. The spectrum of T_z was computed, and the wavenumber where it enters the high-frequency noise floor was determined as outlined in the appendix. All wavenumbers higher than the noise-floor intersection were set to zero. The remaining low wavenumbers were corrected for temperature probe time response (see the appendix) while taking care not to distort the various measures of mean gradient. The spectrum was then integrated to find the mean-square gradient over the 0.5-m bin; this is the sum of the squared mean gradient plus the gradient variance that goes into χ.

Errors arise in χ because the time response of the probe is imperfectly known; uncertainty in probe response could potentially cause up to 15% error in $\langle \chi \rangle$ (see the appendix). Also, $\langle \chi \rangle$ depends on the method used to remove the noise. The method used here of integrating the spectrum up to a modeled noise floor, without any attempt to remove the noise floor, leads to an additional 1% uncertainty.

The data indicates that probe 2 became fouled after 26 profiles (see the appendix and Fig. 12). Although not catastrophic, this causes $\langle \chi \rangle$ from probe 2 to be 25% lower than from probe 1. The pdfs of the two probes have no significant difference in shape. To avoid confusion, results are reported here only for probe 1 unless stated otherwise.

Values of $\langle \chi \rangle$ corresponding to different mean gradients are listed in Table 1. These were estimated by averaging over 23 000 nonoverlapping 0.5-m bins. Although the estimators use quite different mean gradients, $\langle \chi \rangle$ only varies by 6% between them all.

The accuracy of the sample average of dissipation depends on both the number of samples averaged and on the correlation between these samples. The nonoverlapping 0.5-m averages are nearly uncorrelated. To show this, the mean product $\langle \chi(z)\chi(z + dz) \rangle \equiv C_{\chi\chi}(dz)$ was computed for spatial lags from $dz = 1$ mm (the sampling rate) to $dz = 150$ m for $z > 200$ m (see Fig. 7), where $C_{\chi\chi}$ is based on the zero mean gradient estimator χ_3 and $C_{\chi\chi}$ was computed in three steps. Using χ values calculated directly from the time series every 1 mm of depth, $C_{\chi\chi}$ was estimated for dz from 1 mm to 1 m. Then χ was averaged over 0.1-m bins, and $C_{\chi\chi}$ was computed for $0.1 < dz < 20$ m. Finally, χ averaged over 0.5-m bins (as above) was used for $0.5 < dz < 150$ m. These 0.5-m averages were also used to compute $C_{\chi\chi}(dt)$ for time lags between profiles for $3 < dt < 240$ hours. The correlation of χ falls to 0.1 by $dz = 10$ cm and decreases to 0.01 by 1 m. The fractional decrease of $C_{\chi\chi}(dz)$ slows near $dz = 10$ m, where its value is near $C_{\chi\chi}(dt)$ for all observed lags. Although many realizations were averaged to form $C_{\chi\chi}$, the averages are dominated by a few large events, resulting in the somewhat noisy curve in Fig. 7. Because the correlation of χ drops to 0.03 by $dz = 0.5$ m and continues to decay, the sampling error for nonoverlapping sequential 0.5-m averages will be only a few percent larger than it would be if the samples were taken from separate profiles at nearby times and locations.

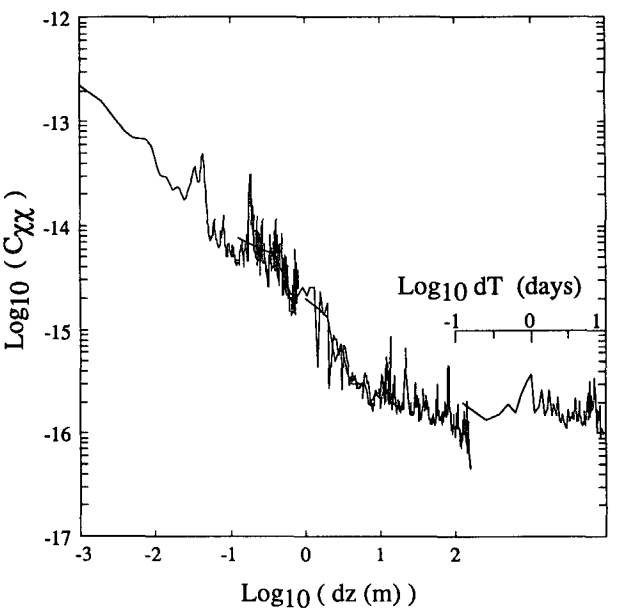

FIG. 7. The mean product of χ, $C_{\chi\chi}(dz)$, is computed for $z > 200$ m for lags $dz = 0.001$–150 m. In addition, time lags are computed from 3 h to 10 days (scales with inset). At $dz = 0.5$ m, $C_{\chi\chi}$ has fallen to ~0.03 of its $dz = 0$ value. For $dz \sim 10$ m, $C_{\chi\chi}$ is equal to its time-lagged values.

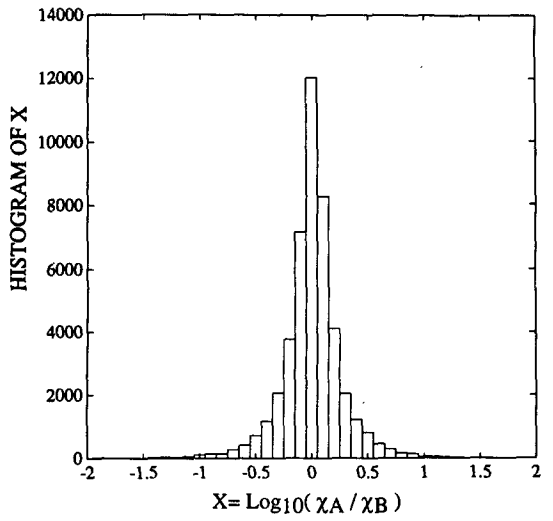

FIG. 8. The ratio of χ from both probes, $R = \chi_A/\chi_B$, has 99% of its values where $0.1 < R < 10$. The asymmetry is due to probe 2 fouling during profile 26, thus biasing R (see the appendix). Bin width of histogram is 0.1. There are a total of 46 000 points. Due to the half-overlap between samples, there are 23 000 independent points.

Given the intermittency of χ, it is difficult to separate a spike of instrumental noise caused by some detritus/biota running into the probe from a real turbulent event (i.e., a salt finger, billow, or initial overturn of a Kelvin–Helmholtz instability). Comparison of the two probes gives some indication of how important such spikes might be. Let χ_A and χ_B be the 0.5-m average χ estimated from probes 1 and 2, respectively, and let R be the ratio χ_A/χ_B. To account for the possibility that sloping isopycnals might cause large χ from the same event to appear in different depth bins for the two probes, R is calculated for adjacent bins and the value closest to $R = 1$ kept. The histogram of R in Fig. 8 indicates that 93% of the time $\frac{1}{3} < R < 3$ and 99% of the time $0.1 < R < 10$. If the 1% of the data where the two χ values differ by 10 are not used, $\langle \chi \rangle$ decreases by 5% for probe 1 and 1% for probe 2. The asymmetry in the distribution of R occurs because probe 2 is fouled during the latter part of the cruise. The occasional lack of correspondence between events in the two probes may result from noise spikes on one probe or from one probe passing through the boundary of a turbulent patch that the other probe misses. Even if all the factor of 10 discrepancies are noise spikes, the effect on the average dissipation is small.

5. The statistics of χ

How reliable is the average dissipation obtained from this dataset? In addressing this, it is important to isolate two kinds of sampling error. The first is caused by the high intermittency of ocean turbulence under a given set of large-scale conditions (internal wave spectrum, large-scale stratification, lateral shear, etc.). This intermittency is the reason that a sample average over a small dataset is more likely to underestimate $\langle \chi \rangle$ than to overestimate it. There are theoretical reasons to expect the statistical distribution of χ for fixed large-scale conditions to be approximately lognormal. This is why Baker and Gibson (1987) suggest estimating the mean by fitting the observations to a lognormal distribution and finding $\langle \chi \rangle$ from the parameters of that distribution. The second kind of sampling error results from changes in the large-scale low-frequency characteristics of the ocean. The consequent variability of χ is sampling error if $\langle \chi \rangle$ is defined by the many-year average appropriate to the diapycnal flux affecting the general circulation but is not an error for the average over a particular time period and region.

The probability density function (pdf) of 0.5-m averaged χ_0 (local mean) over the 76 profiles shown in Fig. 9 is indeed strongly intermittent and approximately lognormal. This figure shows that a substantial fraction of the total dissipation results from large events. Baker and Gibson (1987) suggest estimating $\langle \chi \rangle$ by plotting the cumulative distribution function (cdf) of $\ln\chi$ on a "normal probability plot" in which a normal distribution appears as a straight line. Fitting a straight line to the observed cdf provides the mean and variance, $\langle \ln\chi \rangle$ and $\sigma^2_{\ln\chi}$, of $\ln\chi$ as well as confidence limits for these parameters (assuming the true distribution is lognormal). This plot for the LAMP data does appear as a straight line over most of its range (Fig. 10). The behavior at low values depends on which $\langle T_z \rangle$ is used. The distributions of all estimators, χ_i, deviate from lognormal for $\chi > 10^{-6}$ K^{2}s^{-1}. Applying Baker and Gibson's graphical method to χ_0, $\langle \overline{\chi_0} \rangle$ is 18% lower

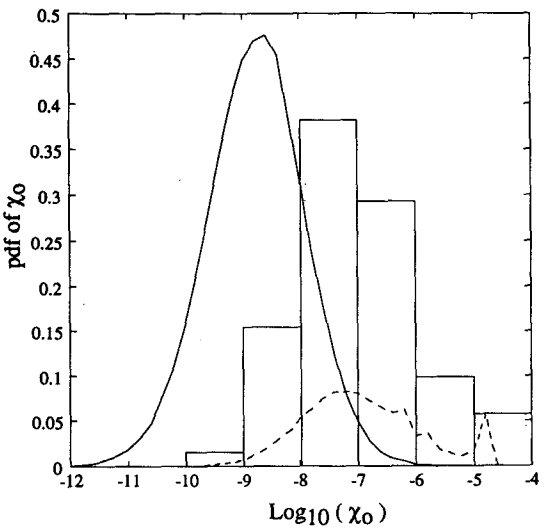

FIG. 9. The pdf of χ, $p(\chi)$, appears lognormal (solid line). Since $\langle \chi \rangle$ is given by the first moment of $p(\chi)$, $\langle \chi \rangle = \Sigma \chi p(\chi)$, the fraction of $\langle \chi \rangle$ determined by $p(\chi)$ is $f = \chi p(\chi)/\langle \chi \rangle$ (dashed line). The value of f is summed over each decade of χ, given by the bar graph, such that values where $-5 < \log(\chi) < -4$ accounts for ~6% of $\langle \chi \rangle$.

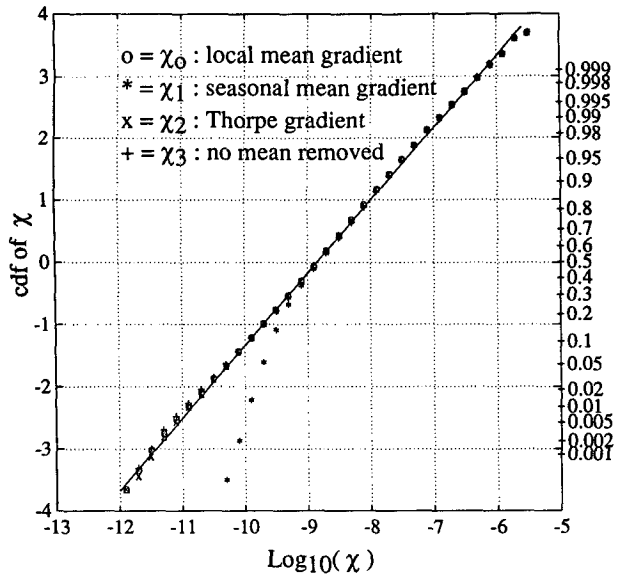

FIG. 10. The cdf of χ is plotted on a normal probability plot, such that if χ is lognormally distributed, it would appear as a straight line above. Left axis denotes number of standard deviations away from the mean value for a normally distributed variable. All four estimates of χ are shown, as marked. All deviate from lognormality at large χ. The plotted straight line is a graphical fit to χ_0, with $\sigma^2_{\ln\chi} = 3.9$.

than the straight arithmetic average from Table 1 with $\sigma^2_{\ln\chi} \approx 3.9$; for a lognormal distribution with $\sigma^2_{\ln\chi} = 4$ the 95% confidence limits for $\langle\chi\rangle$ from 23 000 independent samples are (0.96, 1.04) of the sample mean.

The graphical fit is subjective, relying on a qualitatively "best" fit to the data. An alternate procedure is to select the lognormal distribution that has the maximum likelihood of producing the observations as a random realization (Gregg et al. 1993 performed similar steps). Following Bendat and Piersol (1986), let the range of $\ln\chi$ be divided into equal width bins and let the true probability of an observation falling in bin i be F_i and the observed fraction of events in the bin be f_i. If the number of events in each bin is large, the quantity

$$\psi \equiv \sum_i \frac{[f_i - F_i]^2}{F_i} \qquad (3)$$

is distributed as a χ^2 variable with degrees of freedom equal to the number of bins less the number of constraints applied in calculating f_i. The probability that a set of f_i was produced by a particular F_i therefore increases as ψ decreases. Assuming the underlying pdf for $\ln\chi$ is Gaussian, a mean and variance for $\ln\chi$ were found by minimizing ψ for $-10 < \log_{10}\chi < -6.4$, thereby avoiding problems at low χ caused by noise and sensitivity to the mean gradient and also ignoring the large-χ tail of the curve that also deviates from the lognormal. For χ_1 a narrower range, $-9 < \log_{10}\chi_1 < -6.4$, is used to avoid the large deviation from a straight line at low χ_1. Values of $\sigma^2_{\ln\chi}$ (Table 1) range between 3.5 and 3.8. With ψ minimized, the resulting fits fail to pass χ^2 tests at a confidence level above 8%–32%, and this level drops below 1%–20% when the entire upper tail of the pdf is included. In other words, if χ were indeed lognormal and the experiment were repeated many times, a distribution that fits the theory as poorly as the observed distribution does would occur only 1%–20% of the time. Values of $\langle\chi\rangle$ based on the different lognormal models are smaller than the arithmetic mean by 9%–18% (Table 1).

Figure 11 shows the measured Cox number, $C_x \equiv \langle\chi\rangle/(2\kappa\cdot\langle T_z\rangle^2) = K_V/\kappa$, obtained by averaging χ and $\langle T_z(z)\rangle$ over 5-m bins. The depth-averaged Cox number $\langle C_x\rangle$ is 98, consistent with $K_V \approx 100\kappa \approx 1.4 \times 10^{-5}$ m^2 s^{-1}. The large value near 220 m arises from a single event in profile 18 (Fig. 6). Without this event, the average of $\langle\chi\rangle$ over all depths would be reduced by 10%, and $\langle\chi\rangle$ for 215–220 m would decrease by 50%. There are ~800 samples per depth bin giving Baker–Gibson 95% confidence limits of (.79, 1.27) for the average in each bin. The observations fall outside these limits 30% of the time suggesting a nonrandom pattern of K_V variation with depth.

Could this pattern of variation reflect the effect of Väisälä frequency N on K_V? For z = 200–350 m, N

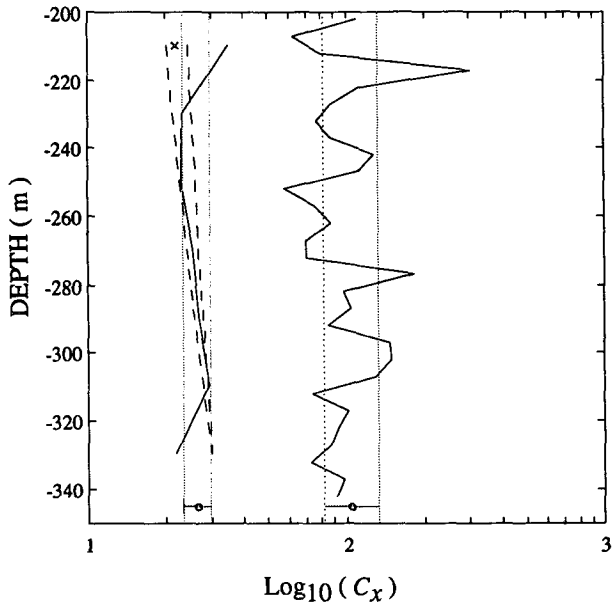

FIG. 11. Plot of C_x estimated in 5-m bins for the 76 profiles, with an average value of 100 (right-hand solid line). Dotted lines represent 95% confidence limits using the Baker and Gibson model. The large value near 220 m is due to the patch in Fig. 6. C_x is also averaged over 20-m bins ($C_x/4$ is plotted, left-hand solid line), with its corresponding confidence limits (dotted lines). Dashed lines represent how C_x would scale with Väisälä frequency using the Gargett and Holloway model, where $C_x = N^p$, with $-1 < p < -0.5$. The "x" represents the 20-m average C_x value ignoring the large event in Fig. 6.

varies from 2.5 to 1.5 cph (see Fig. 3). According to the Gargett and Holloway (1984) model, C_x should vary as N^p with $-1 > p > -0.5$, causing C_x to increase 30%–66% from 200 to 350 m. Neither the observations averaged over 5 m nor 20 m (Fig. 11) can confirm this. Regression analysis suggests there is no significant correlation between N and C_x. The 20-m averages have tighter confidence limits and between 230 and 310 m C_x falls between the expected -0.5, -1 slopes. The single event in profile 18, however, makes C_x above 230 m so large as to disagree with the Gargett–Holloway theory with 95% confidence. The small values below 310 m are also, by the lognormal distribution, significantly different from the model. We must conclude that the observations are unable to explain how K_V varies with depth or with N. The observed K_V profile may result from an unexplained pattern of variation or from statistical variation that is larger than expected from the natural variability of χ. Averaging over more profiles and/or greater range in N will be required to determine which with statistical confidence.

There is also an apparently significant variation of $\langle\chi\rangle$ with time. Figure 12 shows χ averaged over $z > 200$ m for each profile and also the Baker–Gibson 95% confidence limits. The profile 18 value is about 10 times larger than the rest, arising from the patch in Fig. 6. For the latter half of the deployment $\langle\chi\rangle$ is about 50% of the average over the first half; this is significant by the calculated confidence limits. This could reflect either natural variability or degradation of the probes. Comparison of $\langle\chi\rangle$ from both sensors shows a step function, with sensor 2 apparently fouling at profile 26, (Fig. 12, the appendix). Since sensor 2 after fouling has a different frequency response (Fig. A1), it more severely attenuates large χ (which has more variance at high wavenumbers), with less bias for low χ. Thus, the two sensors agree better at small χ values. From Fig. 12 it appears as though there is only one large fouling event. Otherwise, the two sensors track the long-term variability in χ within the expected sampling uncertainty. To explain the long-term variability by fouling requires synchronous fouling or sensor degradation. Modeling of biomass distribution leads to $\sim$1% probability that both sensors would foul versus just one (the appendix). Since only one fouling event is apparent, it seems unlikely (but certainly not impossible) that dual fouling occurred.

In conclusion, the 23 000 nearly independent estimates combined with a nearly lognormal distribution give 95% confidence limits of $\pm$4% for the deployment-average $\langle\chi\rangle$. Similar variability arises from how the mean gradient is defined ($\pm$3%). Uncertainty in probe transient response adds $\pm$15% uncertainty. Additionally, 1%–5% of dissipation occurs in high χ events seen in one probe but not the other and may represent noise spikes. Assuming strict isotropy, the vertical eddy diffusivity is $K_V = 100\kappa = 1.4 \times 10^{-5}$ m^2 s^{-1} with error bounds near $\pm$17%. Sampling uncertainty within the time and depth range investigated is not a significant factor in this uncertainty.

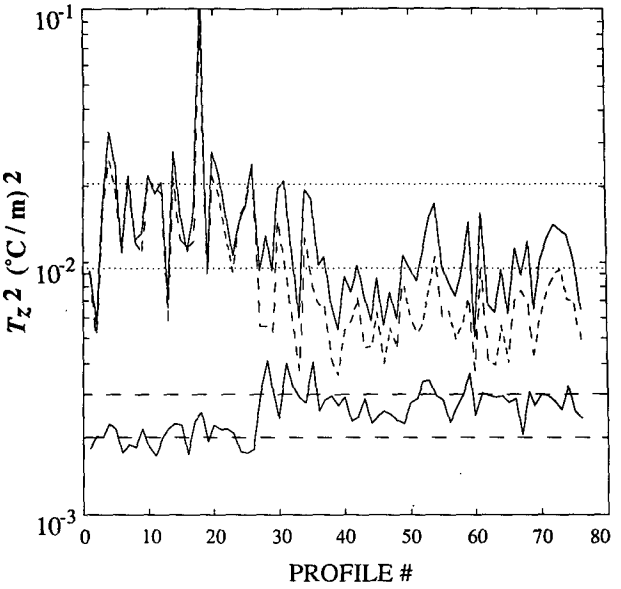

FIG. 12. Plot of T_z^2 averaged for $z > 200$ m for each profile for both sensors (solid line: sensor 1, dashed: sensor 2). After profile 26, variance of sensor 2 falls to 65% of sensor 1 for the remainder of the deployment. The dotted lines represent 95% confidence limits on the mean value of T_z^2 for each profile, assuming lognormal statistics (Baker and Gibson 1987). Thus, the reduction of variance in the latter half of the cruise is statistically significant. The lower solid line is the ratio of T_z^2 of sensor 1/sensor 2, with dashed lines given as references.

Fitting the data to a lognormal distribution reduces the estimated $\langle\chi\rangle$ by 9%–18% (Table 1). We have observed more high χ events than expected from a lognormal distribution. That the lognormal model underestimates $\langle\chi\rangle$ by more than its own 95% confidence limits suggests that the model does not represent the data. Much of the variability not accounted for by the lognormal model appears to represent a consistent pattern of change in time and perhaps depth. Here χ decreased by a factor of 2 over the 10-day observation and time averages at different depths differ by more than the apparent statistical uncertainty. Some of this variability may be due to sensor fouling, although it seems unlikely that probe degradation accounts for all of it (the appendix). It is quite possible that variability of this sort is the primary difficulty in establishing the long-term average K_V appropriate to the general circulation.

6. Isotropy

The preceding calculation of $\langle\chi\rangle$ assumed isotropy by setting $\Gamma = 3$ in (2). This approximation potentially overestimates $\langle\chi\rangle$ by a factor of 1–3. Gargett et al. (1984) addressed anisotropy by comparing cross-stream and streamwise velocity spectra for varying dissipation rates. They found that the degree of isotropy

depended upon the ratio of the Kolmogorov wavenumber $k_s = [\epsilon/\nu^3]^{1/4}$ and the buoyancy wavenumber $k_0 = [N^3/\epsilon]^{1/2}$ (ϵ: kinetic energy dissipation rate, ν: kinematic viscosity). The ratio $k_s/k_0 = [\epsilon/(\nu N^2)]^{3/4}$ represents the range of scales available for the development of the inertial subrange. Gargett et al. observed a departure from dissipation-scale isotropy for $\epsilon < 200\nu N^2$. For typical oceanic values of $\langle\epsilon\rangle$ they concluded that large dissipation events are isotropic so that no significant correction of $\langle\epsilon\rangle$ is required. Itsweire et al. (1993) conducted a numerical simulation study and found significant anisotropy at dissipation-scale, even for $\epsilon > 200\nu N^2$. Their simulation was for low Reynold's numbers (Re_λ = 26–104, where λ is the Taylor microscale), which might lead to the discrepancy with the Gargett et al. results. They also observed that isotropy was more strongly influenced by the strength of the shear flow than by the stratification. They concluded that anisotropy could reduce observational values of K_ν by a factor of 2.

Anisotropy is investigated here using the difference between the two probes to characterize $T'_x{}^2$. Over the 0.5-m depth bins, T_x and T_z were calculated for $dx = dz = 0.18$ m. The 0.5-m average values were removed and the resulting $\langle T'_x{}^2\rangle$ computed. Subtracting the 0.5-m mean coupled with the $dx = dz = 0.18$-m separation is equivalent to applying a bandpass filter causing the gradient variances to be dominated by 0.5–0.18-m scales.

Let the horizontal-to-total variance ratio F be defined as $F = \langle T'_x{}^2\rangle/(\langle T'_x{}^2\rangle + \langle T'_z{}^2\rangle)$. The associated degree of isotropy is $I = (1 + F)/(1 - F)$ with $I = 3$ for isotropy ($F = 0.5$). Here F can be interpreted in two ways: If T is taken as $T = T_0\exp[i(kx + mz)]$, then $F = k^2/(m^2 + k^2)$ is a measure of the aspect ratio of the small-scale temperature field. Alternatively, the T field could be completely stratified but tilted at the angle θ to the horizontal. Then $T'_x{}^2 = T'^2\sin^2\theta$, $T'_z{}^2 = T'^2\cos^2\theta$, and $F = \sin^2\theta$ is a measure of the tilting. If $F = 0.5$, then either the flow is isotropic or the local tilting is of order 45°. The deployment mean for $z > 200$ m is $\langle F\rangle = 0.38$, equivalent to $\langle I\rangle = 2.25$, or rms tilting of 38°. For a stratified ocean of constant N and no background shear, Thorpe (1978) argues that advective instability will arise for average slopes greater than 14°, equivalent to $F \approx 0.06$. Values of $F > 0.06$ therefore suggest that the temperature variability is indeed due to small-scale flows (or shortly will be).

Values of F, I, and isotropy-corrected χ are calculated over 0.5-m depth bins, leading to a new estimate of $\langle\chi_0\rangle$ 27% lower than the value in Table 1. This is equivalent to using $I = 2.2$ instead of the value 3. This estimate is biased since it is calculated from scales larger than 0.18 m, and therefore does not represent the degree of isotropy at higher wavenumbers, which contain most of the variance. Osborn and Lueck (1984) compared velocity spectra and found anisotropy to be a function of wavenumber, with full isotropy at dissipation scales. Therefore, reducing the $\langle\chi\rangle$ based on isotropy should produce a lower bound.

As stated above, the degree of isotropy should be correlated with $[\epsilon/(\nu N^2)]^{3/4}$. Assuming a balance between turbulent production and viscous dissipation combined with a constant mixing efficiency γ, the Cox number can be related to ϵ as $C_x = \epsilon\gamma/\kappa N^2$ (Osborn 1980). Using this relation, $\epsilon/\nu N^2 = C_x/\gamma\mathrm{Pr}$, (Prandtl number $\mathrm{Pr} = \nu/\kappa$), and we expect I to be correlated to C_x. Calculations of I and C_x over individual 0.5-m depth bins likely violate the above basic assumptions since production and dissipation are not necessarily in balance for each single realization. Additionally, γ depends upon the balance between buoyancy flux and turbulent production, which will also not be constant over 0.5 m realizations. Nevertheless, undaunted, we investigate the correlation between F and C_x.

For each 0.5-m estimate, C_x was calculated using the local temperature gradient: $C_x = \chi/(2\kappa\cdot\overline{T}_z{}^2)$. The correlation was computed between $\log(F)$ and $\log(C_x)$, yielding a low value of $\rho = 0.13$. The plot of the conditional pdf between F and C_x shows this weak correlation, more pronounced for the lower bound on F (Fig. 13a). This suggests high C_x events tend to be slightly more isotropic than low C_x values, which display wider variability.

The relation between F and C_x provides a rather dubious confirmation of our assumptions. One obvious fault is that in the definition of C_x the local gradient is used, which will underestimate the background gradient when there are overturns of the same scale as the averaging size of 0.5 m. This suggests using the Thorpe gradient G_T instead, forming an effective

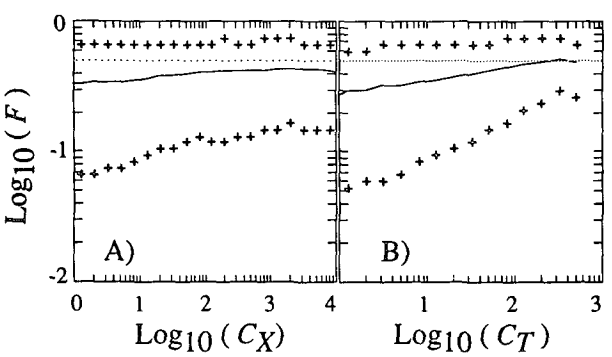

FIG. 13. (a) The conditional pdf between the horizontal-to-total variance ratio F and the Cox number is shown. The solid line refers to $\langle F(C_x)\rangle$ (mean value of F, conditional on C_x). The upper and lower values of F, such that 10% of all values of $F(C_x)$ are above the upper limit, and 10% are below the lower limit, are marked with +s. If F and C_x are uncorrelated, $\langle F(C_x)\rangle$, along with the 10% limits, should be independent of C_x. There is a weak correlation, best seen by the dependence of the lower limit on C_x. (b) The same as (a) except using the Cox–Thorpe number C_T. Note the stronger correlation, particularly exemplified by the lower limit dependence on C_T. Although there is wide scatter in F at low C_T, this is significantly reduced at the highest C_T values. The dotted line marks $F = 0.5$, equal to full isotropy ($I = 3$).

Cox number, labeled here as the Cox–Thorpe number $C_T = \chi/(2\kappa \cdot G_T^2)$. Dillon (1982) defined his local Cox number in a similar way.

A simplistic explanation gives a more intuitive meaning for C_T. The Thorpe gradient represents the largest potential gradient possible over the 0.5 m, that is, what would be present in the absence of all small-scale motions. We can therefore use G_T as the 0.5-m estimate of the background gradient. Let the Fourier components of T'_z be defined as $T'_z(k) = G_T \cdot \xi(k)$, where $\xi(k)$ represents the wavenumber distribution of the finestructure. This says we can have the same fine-structure pattern between two patches, with the only difference being the value of the background gradient. Thus, $\chi = G_T^2 \int \xi^2(k) dk$ depends upon both the magnitude of G_T, which is distorted by the turbulence, plus the dissipation rate, which pushes T'_z variance into higher wavenumbers. By dividing χ by G_T^2, the effect of G_T is removed, and C_T is an estimate of the high wavenumber variance. If the overall spectral shape is the same between 0.5-m realizations (i.e., the Batchelor spectrum), then an increase of C_T does not necessitate a balance of turbulent production and dissipation, but simply serves as an estimator of the smallest scales of the turbulence.

Correlation between $\log(F)$ and $\log(C_T)$ is $\rho = 0.23$. Although this correlation is still low, it is higher than that obtained using C_χ. This higher correlation is most evident for the 10% lower bound in the conditional pdf plot (Fig. 13b). Low C_T events have a more variable degree of isotropy, whereas high C_T values are rarely anisotropic.

The potential effect of anisotropy is to lower $\langle \chi \rangle$ by as much as 27%. Due to isotropy not actually being measured at high wavenumber, the estimate defines the lower bound. The degree of isotropy appears to be best correlated with C_T. This relation will be exploited in the next section.

7. The Batchelor spectrum

The Osborn–Cox model provides an estimate of the diapycnal eddy diffusivity K_V by balancing the production of temperature variance against its dissipation at molecular scales. Although predicting K_V, this approach does not provide insight into how the variance is cascaded to smaller scales. In a sense, this is an advantage because it does not require particular dynamical conditions to be met for the model to apply. All that is required is that accumulation and turbulent fluxes of $\langle T'^2 \rangle$ be unimportant and that production be dominated by the diapycnal flux. If these conditions are met, the model applies to fluxes supported by breaking internal waves, double-diffusive convection or intrusions.

Batchelor (1959) predicted a theoretical universal temperature spectrum for homogeneous, locally isotropic, unstratified, turbulent flow. The Batchelor spectrum depends on the physics of the energy flux, breaking the spectrum into three regimes. Low wavenumbers are an inertial subrange where the velocity field is not affected by viscosity and the classical Kolmogorov cascade results in a $k^{1/3}$ spectrum for T_z. This is followed by a viscous–convective range where velocity, smoothed by viscosity, strains the temperature field and produces a k^1 spectrum for T_z. At the Batchelor wavenumber, $k_B = (\epsilon \nu^{-1} \kappa^{-2})^{1/4}$, thermal conduction becomes important and causes an exponential rolloff of the spectrum at higher wavenumbers. The shape of the spectrum is invariant to the dissipation rate, but the location of k_B relative to the spectrum's peak depends on a universal constant q that scales the rate of straining in the viscous–convective range. The Batchelor spectrum plays three potential roles for oceanic microstructure. It relates the temperature field directly to the dissipation of kinetic energy through K_B and provides a model for the energy flux to smaller scales. It also defines the length scale that must be resolved before thermal dissipation can be accurately measured.

The ocean is strongly stratified with intermittent turbulence having a variable degree of isotropy so the applicability of the Batchelor spectrum is uncertain. Dillon and Caldwell (1980) found T_z spectra to be in good agreement with the general shape of the Batchelor spectrum. They did this by normalizing spectral amplitudes and wavenumbers before averaging and by sorting spectral estimates according to the local Cox number C_χ. In the process of normalizing, information is lost on Batchelor's constant q. Dillon and Caldwell found that all spectra display the dissipative exponential decay at high wavenumber, with the +1 slope in the viscous–convective range holding for only high C_χ events. Their dataset is from the mixed layer as well as the thermocline, includes dissipation events 100 times larger than observed by LAMP, and therefore covers a much broader range of C_χ.

Gargett (1985) measured both the velocity and temperature fields, allowing direct estimates of isotropy, ϵ, and k_B. She found that T_x spectra did not obey a Batchelor form for the most isotropic velocity events, including in the dissipation scale, where the estimated q was 12, rather than the canonical value of 4. The T_x spectra only tended toward the Batchelor spectrum when the velocity field was anisotropic (at low values of $\epsilon/\nu N^2$, and thus presumably for low C_χ). The contradiction of Gargett's results with those of Dillon and Caldwell is perplexing. It either implies that Cox numbers based on T_x and T_z are not well correlated (therefore T is anisotropic), or that instantaneous estimates of C_χ do not necessarily scale with ϵ. A direct comparison of T_z with the Batchelor spectrum requires knowing ϵ so that, unfortunately, Gargett's results cannot be verified with our data.

The Dillon and Caldwell (1980) approach is explored here with a much larger dataset. The one-di-

mensional wavenumber spectrum $S(k)$ of T_z was computed for every 0.5-m subrecord using a Hanning window and 0.25-m overlap between estimates. To determine the parameters used for normalization before bin-to-bin averaging, the spectrum was smoothed by averaging seven consecutive wavenumbers to form $\tilde{S}(k)$. To minimize the effect of noise, only spectra with large dynamic range, defined as maximum-to-minimum ratio of at least 20, are used for averaging. These spectra are scanned to find the wavenumber k_{max} at the maximum of $k\tilde{S}(k)$ and the spectral amplitude normalized to $\Phi = S(k)/S(k_{max})$. Then $\tilde{S}$ was scanned to find the wavenumber $k_c > k_{max}$, where the spectrum rolled off to 0.1 of its peak value. The normalized spectrum at fixed normalized wavenumber $m = k/k_c$ were then averaged over categories defined by the Cox–Thorpe number C_T. Each $S(m)$ was cut off at its noise floor (see appendix) so that the maximum wavenumbers vary. At large m the average of $\Phi(m)$ is computed from fewer individual spectra with low signal to noise ratio and some residual noise contamination is evident.

The normalization technique for finding the maximum value of $k \cdot S(k)$ constrains the normalized spectrum to roll off with a slope steeper that k^{-1} to its $S(k_c) = 0.1$ value. Other schemes were tested, including normalizing by the maximum value of $S(k)$ and by the total variance, and the results were essentially unchanged.

Normalized spectra are computed from sensor 1 for all $z > 200$ m. These were sorted by C_T, which has already been shown to be correlated with isotropy in section 6. Four estimates of $\langle \Phi(m) \rangle$ were made for the following subsets of C_T: (i) all values of C_T (3960 individual spectra averaged), (ii) $C_T > 100$ (1240 spectra averaged), (iii) $C_T > 150$ (511 points), and (iv) $C_T > 190$ (88 spectra averaged). The four subsets are not mutually exclusive, so for example spectra averaged in group (iii) include those in (iv). Each spectral density was averaged over 8 cycles per m (4 estimates in k) so that the number of degrees of freedom in $\langle \Phi(m) \rangle$ is 8 times the number of spectra averaged. In addition to $\langle \Phi(m) \rangle$, a histogram of spectral densities for each m was calculated to define upper and lower bounds such that 80% of all individual spectra lie between these bounds. This envelope is used to describe the variability between individual spectra. If the normalized spectra are shape invariant and T_z is approximately normally distributed, then spectra should correspond to a χ^2_8 variable with 80% lower and upper bounds of $(0.43, 1.67) \times \langle \Phi(m) \rangle$.

Averages of $\langle \Phi(m) \rangle$ for all four ranges of C_T display a steep dissipative rolloff at high wavenumber (Fig. 14, $m > 0.7$). At large m, noise contamination interrupts the dissipative rolloff. At low wavenumbers a nearly flat $\langle \Phi(m) \rangle$ is seen for the average over all C_T, similar to Dillon and Caldwell's average for all Cox numbers. As averaging is limited to higher and higher values of C_T (>100, 150, 190), the resulting low-wavenumber

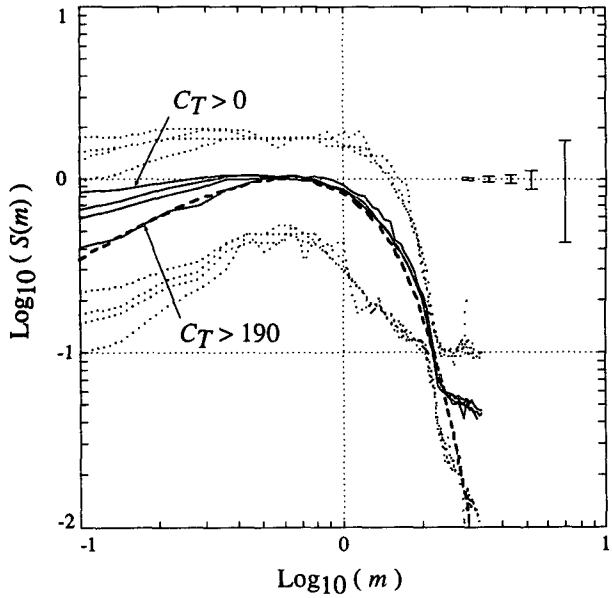

FIG. 14. Normalized T_z spectra $S(m)$ for various subsets of C_T values (solid lines) are compared with the Batchelor spectrum (dashed line). Dotted lines represent where 10% of the spectral density values lie above/below the lines, such that 80% of all values lie between the dotted lines. Spectra are computed for all C_T, $C_T > 100$, $C_T > 150$, and $C_T > 190$. As C_T is constrained to higher and higher values, the low wavenumber slope steepens, approaching Batchelor's viscous–convective region at the highest C_T. All spectra exhibit the exponential decay at high wavenumbers. The 98% confidence limits are shown for the far normalized spectra, with the largest error bars for $C_T > 190$. Also on the far right is the 80% sampling bar for each individual spectrum, such that the 80% measured dotted lines should agree if the underlying shape is stationary.

slope increases, approaching the slope of the Batchelor spectrum for $C_T > 190$. This last average is over only 88 spectra, and represents the upper limit of C_T for which reliable averages can be computed from this dataset. As with the results of Dillon and Caldwell, a viscous–convective range is observed only for the highest Cox number events, with a high-wavenumber exponential decay seen on the averages for all Cox numbers.

If on average C_T is related to ϵ by $C_T = \epsilon\gamma/\kappa N^2$, and $\gamma = 0.2$, then ϵ and k_B can be computed, and m can be given dimensional units. For $C_T = 100$–200, the 18-cm probe separation corresponds to $m = 0.2$–0.17. This range of m only agrees with the Batchelor spectrum for $C_T > 190$ (Fig. 14). From Fig. 13b, full isotropy as measured between the sensors is observed on average for $C_T > 200$–300. This implies that isotropy at low wavenumbers is reached as the Batchelor spectrum is approached.

Although the average spectra exhibit dissipative rolloffs similar to the Batchelor spectrum, individual spectra do not necessarily follow the Batchelor form. The spectral deviations are not due to sampling uncertainty alone, but represent actual physical features. Secondary peaks are sometimes embedded in the rolloff

region, and in different examples the spectra decay at different rates. Lack of uniformity between spectra severely limits the ability to estimate k_B, and thus ϵ (which depends on k_B^4), directly from the spectra.

The Batchelor spectrum is apparently a useful tool to define the wavenumbers (near k_B) where oceanic dissipation is significant. For a given ϵ, this sets the smallest length scale that must be resolved to measure χ (cf. Gregg 1987). While the average spectra in certain oceanic regimes may approximate the Batchelor spectrum, the variability between individual spectra precludes matching individual spectra to the Batchelor form. Indeed, Gargett's (1985) results suggest that Batchelor's universal constant q is actually variable. Even when the diffusive range matches the Batchelor form, q must be known before estimating k_B and thus ϵ.

8. Conclusions

LAMP is an autonomous profiler capable of gathering $O(100)$ microtemperature profiles over a duration of several months. In its first deployment in May 1992 it collected 76 profiles to 350-m depth over ten days.

The average thermal dissipation rate $\langle \chi \rangle$ was measured and the potential errors in this average examined. Imperfectly known probe time response makes $\langle \chi \rangle$ uncertain by 15% of $\langle \chi \rangle$. Mean χ was estimated using four different estimators for the background temperature $\langle T_z \rangle$ with results that differed by 3%. The pdf of T_z is approximately lognormal, with the highest deviation occurring at the upper tail of the pdf. Using approximate lognormality to estimate confidence limits for the deployment-average $\langle \chi \rangle$ (as Baker and Gibson 1987) gives 95% limits of ±4%. This shows that it is feasible to sample χ completely enough that statistical uncertainty from local intermittency is relatively unimportant.

Two probes, separated horizontally by 0.18 m, recorded microtemperature. If χ values are ignored when the two probes disagree by a factor of 10, $\langle \chi \rangle$ is decreased by 1%–5%. Using the two probes to estimate anisotropy shows that assuming isotropy overestimates $\langle \chi \rangle$ by less than ~30%. Since isotropy is based on 0.18-m scales, the actual error is likely much less than 30%. Isotropy does show some correlation with the Cox number and a better correlation with the Cox number formed from the local Thorpe gradient (denoted here by the Cox–Thorpe number C_T).

The experiment average dissipation is $\langle \chi \rangle = 1.2 \times 10^{-8}\ \mathrm{K^2\ s^{-1}}$, corresponding to a mean Cox number of 98 and a vertical eddy diffusivity of $K_V = 1.4 \times 10^{-5}\ \mathrm{m^2\ s^{-1}}$. Uncertainties from the probe response, anisotropy, and possible noise glitches (where both probes disagree by a factor of 10) place loose error bounds of ±22% on K_V, completely outweighing the 4% sampling uncertainty due to quasi-lognormal intermittency.

More importantly, χ decreases by 50% between the first and second half of the deployment. This long-term temporal variability (not to be confused with the intermittency that is quasi-lognormal) causes much more uncertainty in $\langle \chi \rangle$ and K_V than statistical uncertainty and estimation technique combined. The unknown is whether this temporal variability is due to natural variance or sensor degradation. Ledwell et al. (1993) estimate the average K_V over two consecutive six month periods, finding K_V to increase by 60%. The LAMP's observed variability in $\langle \chi \rangle$ is within bounds of what is expected naturally. However, it could also arise from continual fouling of both sensors over a few-days period. Although the characteristic of the decrease of χ does not seem likely from fouling (see appendix), it is still a possibility. Future calibration of the thermistor transient response immediately after recovery would at least give an indication of the amount of sensor degradation. A system to clean the sensors between profiles would be best. In situ calibration might be possible with a stream of water heated by a high-frequency pulsed source or by running the thermistor as a hot-film.

The above estimate of K_V can be compared with Ledwell et al. (1993), who find $K_V = 1.1 \times 10^{-5}\ \mathrm{m^2\ s^{-1}}$ based on the tracer's diffusion over the initial six month time period of the NATRE experiment. The LAMP results are consistent with this, given the error bounds for the microstructure analysis and the temporal variability of χ over the ten-day deployment (as seen in Fig. 12).

Normalizing spectra of T_z gives an average that agrees with Batchelor's (1959) dissipative rolloff. A viscous–convective range is, however, found only for the events with the highest Cox number. Variability of individual spectra from the Batchelor form precludes using an estimated k_B to infer ϵ.

LAMP's ability to autonomously collect temperature microstructure over many profiles over a long time allows an estimate of K_V that is constrained by instrumental uncertainty and estimator technique but not statistical uncertainty from local intermittence. However, K_V varies smoothly by a factor of 2 from the first to the last half of the present ten-day observation. Long-term deployments are needed to describe seasonal, and other low-frequency, variability of the thermal dissipation rate. Additionally, a seasonal average would allow a better comparison with the Gargett and Holloway (1984) hypothesis of a depth-dependent vertical diffusivity or other parameterizations of K_V. Perhaps the biggest obstacle in interpreting a seasonal record from LAMP is quantifying the amount of thermistor degradation due to biological fouling.

A disappointing afternote: LAMP was lost on an eight-month mission during the second half of NATRE. It apparently failed to surface at mission's end, perhaps because of a pump part found faulty in a number of other ALACE instruments. This under-

scores the risk of using an autonomous instrument that must be weighted against the potential reward of a long-term microstructure record.

Acknowledgments. Mike Gregg encouraged us and made both his instrument AMP and his time available during engineering tests of LAMP. Jim Ledwell graciously allowed LAMP to hitch a ride as a last-minute addition to the initial NATRE tracer release cruise. Ann Gargett provided many useful ideas during review. This work was funded by Office of Naval Research Grant N00014-89-J-1046.

APPENDIX

Thermistor Performance and Noise Analysis

a. Analysis of sensor fouling

On recovery from the May 1992 deployment, one sensor had some biofouling at the base of the thermistor. Inspection of T_z variance levels between sensors, averaged for depths > 200 m for each profile, shows that after profile 26, variance of sensor 2 falls to 65% of the sensor 1 value (Fig. 12). Frequency spectra for both probes are averaged over $z > 200$ m for each profile, with spectra compared before and after profile 26. The change in response of sensor 2, as compared to sensor 1, is similar to a single-pole filter with a −3 dB point at 8 Hz (Fig. A1). If the attenuation was due to a uniform layer of contaminant, its thickness would be $L = (\kappa t)^{1/2} = [\kappa/(2\pi f)]^{1/2}$, where κ is the contaminant thermal diffusivity and f is the e-folding frequency. Taking κ equal to that of water and $f = 8$ Hz yields a thickness L of order 0.05 mm. Fouling by such a small thickness seems reasonable.

The question arises if sensor 1 was also fouled at the same time, and whether the resulting degradation could be responsible for the long-term temporal variability of χ as seen in Fig. 12. The ratio of χ_1/χ_2 in Fig. 12 appears as a step function, implying that only one large fouling event occurred. If other fouling took place, it was either of smaller magnitude, or affected both sensors to the same extent. Unfortunately, the natural variability in χ makes detecting small fouling events difficult. The major decrease in χ_1 occurs between profiles 26 and 38, equal to a 36-hour period, and does not appear as a step function, indicating either multiple fouling or true natural variability. One can play devil's advocate and suggest both sensors fouled at the same time. If the peak of χ_1 near profile 35 is matched to the peak near profile 20, the resulting time series would still appear reasonable, implying that χ_1 could have been simultaneously fouled, with its level decreased by 30%. Potentially at least half the long-term temporal variance may be due to simultaneous fouling during profile 26.

We cannot ascertain if the drop in χ for the second half of the cruise is due to oceanic variability or fouling. However, we can discuss the probability of both sensors fouling versus just one.

Possible sources for fouling include jellyfish and zooplankton. Some types of zooplankton construct a mucus-based feeding structure, complete with intake screens and an internal filtering system. Barham (1979) notes that these structures, commonly referred to as "houses," can be an order of magnitude larger than the animal itself. Barham observed giant larvacean houses of order 70–100 cm diameter in eastern Pacific coastal waters, although Alldredge and Silver (1988) note that the most common house size is 0.1–2 cm in diameter. They further discuss that individual zooplankton can produce and discard upward of 4–16 houses a day (the house is abandoned when the filters become clogged), taking up to six days before the house disintegrates (Davoll and Silver 1986). Therefore one animal could potentially be responsible for 100 houses, ten times the size of the creature, in the water column at any one time. Given that these are a mucus-based structure, they are perfect for fouling thermistors. They also have the potential size to foul both sensors simultaneously.

The probability of both sensors fouling versus one will be modeled as follows. Let a be the diameter of the plankter, of which there are $n(a)$ plankton within a horizontal cross section with diameter D, which encompasses both probes. The probability of one plankter of size a hitting either probe can be given as a ratio of cross-sectional areas:

$$ps(a) = 2(a - 0.5)^2/D^2, \quad a > 0.5 \text{ cm}. \quad \text{(A1)}$$

The minimum cutoff at 0.5 cm represents the base diameter of the sensor, with the assumption that smaller particles will not foul the probe, but will tend to follow the laminar flow to either side of the probe. The multiplication of 2 is due to having two probes in the volume. The probability of any a-sized particle hitting the probe is simply $PS(a) = n(a)ps(a)$. Likewise, for simultaneous fouling of both probes to occur, we have

$$PD(a) = n(a)(a - 18)^2/D^2, \quad a > 18 \text{ cm}, \quad \text{(A2)}$$

where 18 cm is the separation between probes. The exclusive set of when only one probe is fouled (but not both) for $a > 18$ cm is given by $PS(a) - PD(a)$. Once $n(a)$ is modeled, $PS(a)$, $PD(a)$ can be integrated to give the probability of single probe fouling versus both.

It has been generally observed that biomass is approximately logarithmically distributed in weight w, (i.e., Rodriguez and Mullin 1986), such that biomass $dB(w) = Aw^{-1}dw$, represents the amount of total biomass from particles of weight $w \pm dw/2$. The number of individuals can be approximated as $n(w) = dB/w = Aw^{-2}dw$. The individual weight will be modeled as a sphere ($w \sim a^3$), giving an estimated particle distribution $n(a) = C_0 a^{-4} da$.

We will consider Barham's (1979) observation of 100-cm houses as typical of the largest size expected, setting a_{max} = (50, 100, 200) cm for the upper limit on the integration of (A1)–(A2). The analytical solutions yield single probe fouling occurring (265, 127, 94) times more often for a_{max} = (50, 100, 200) cm. From Fig. 12, there is only one obvious instance where single fouling occurred, with the mucus sticking for the rest of the deployment. The odds of this one fouling event hitting both sensors versus only one would appear low, on the order of 1%.

The model is questionable since it is not clear what species are even present at the LAMP site. The dominant species at time of deployment may not follow the logarithmic biomass distribution (i.e., if most of the individuals are juveniles). Furthermore, the species might tend to aggregate such that the horizontal cross section of the school leads to increased likelihood of dual fouling. Or perhaps the larger houses/jellyfish are more "sticky" and therefore more likely to create a long-lasting fouling problem.

Besides the individual fouling events which can occur, there may be long-term degradation (i.e., algae growth on the thermistor). This should affect both sensors equally, appearing as a long-term trend to lower values. Between profiles 35 and 50, χ_1/χ_2 decreases, suggesting sensor 1 is degrading (Fig. 12), perhaps the result of multiple fouling or growth on that sensor. However, this is probably an artifact of the observed lower χ values. Since the sensor s/n 2 response suffers at high frequencies (Fig. A1), it will underestimate more severely high χ events, where there is more variance at high wavenumbers. Likewise, during small χ values, which primarily only have variance in low wavenumbers, sensor 2 will be in better agreement with sensor 1.

Approaches must be considered to identify both long-term degradation and discrete fouling episodes. Thermistor sensors should be immediately inspected after recovery. Probe time response should be measured before cleaning the sensor, allowing pre- and postcalibration comparison. Cleaning of the sensors during deployment could be done with a pumped jet of water, say at the end of each profile, although it is not clear whether this by itself would be adequate. Perhaps one can make the water jet's high-frequency characteristics reproducible enough to allow comparison of the sensor's high-frequency response between profiles. This might be done with a pulsed heater in the jet. Likewise, running the thermistor as a hot-film at the end of each profile may yield a quantitative estimate of the amount of fouling.

b. *Noise removal scheme*

Spectra of T_z are contaminated by noise at high frequencies. To investigate the characteristics of this noise, spectra are computed over 2-m scales (2048 data points

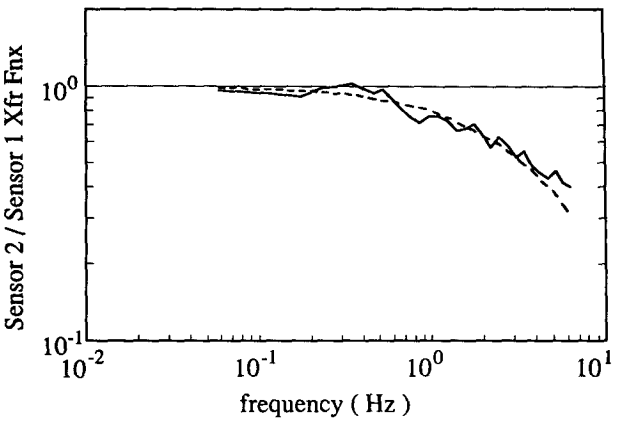

FIG. A1. Average spectra were computed for both sensors for each profile for $z > 200$ m. The ratio of these spectra represents a comparison of the frequency response between both probes. Change in response of probe 2 compared to probe 1 is averaged over all profiles after profile 26, where it is now attenuated at high frequencies (solid line). Behavior is similar to a single-pole filter with a −3 dB point at 8 Hz (dashed line).

Fourier transformed, spectra averaged over 16 successive estimates in frequency). For each profile, the minimum, average, and maximum spectral density values are calculated for $z > 200$ m. These are averaged over the 76 profiles (Fig. A2). All spectra fall into the noise floor before reaching the Nyquist frequency of 30 Hz. The sharp spectral rolloff is due to both the dissipative nature of the ocean and the response of the thermistor.

The contribution of noise to T_z is removed by only integrating T_z spectra out to the noise floor. For each individual spectrum, it is necessary to determine when the spectrum falls into the noise. The shape of the noise floor is modeled from the minimum spectrum (Fig. A2). The noise floor level is set to the expected upper limit. This is estimated by the value of the maximum spectrum at the highest frequencies (Fig. A2). Thus, the modeled noise floor represents the upper bound of the measured noise. When an individual spectrum falls below this noise level, the remaining high-frequency spectral values are set to zero. The lower frequencies are corrected for probe response, and the spectrum is integrated to give the estimate of T_z^2.

Note that no estimate of the noise floor is removed. The modeled noise floor is simply used to define when an individual spectrum is in the noise. This biases χ in two ways. The cutoff throws away both signal and noise at higher frequencies, thus underestimating total variance. Additionally, the lower frequencies just before the cutoff have no noise removed, such that they overestimate the variance. A cutoff frequency is used here instead of trying to remove the noise floor to avoid potentially large noise problems at high frequencies. This arises when the probe time response correction is made, which can significantly amplify noise at the highest frequencies (gain due to probe response is ~15 at 30 Hz).

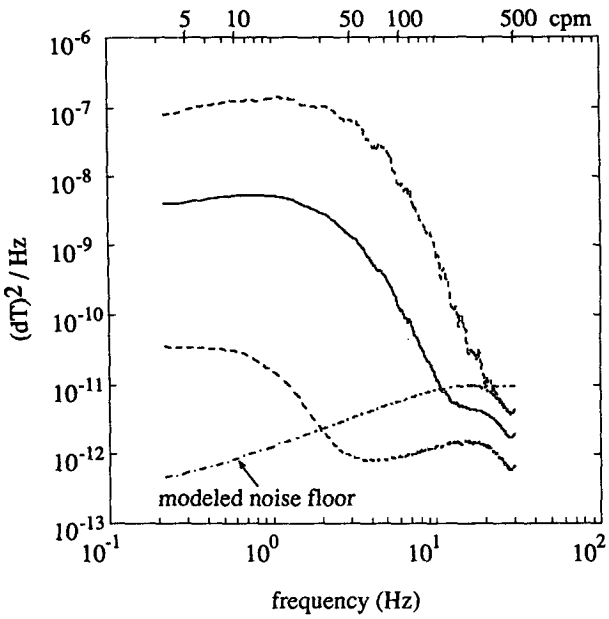

FIG. A2. Average spectrum of T_z is computed over all profiles for $z > 200$ m (solid line). The maximum and minimum spectral values for each profile are also averaged over all profiles (dashed lines). The profile-averaged minimum spectrum is used to model the shape of the noise floor (dash-dot), with its level set by the maximum spectrum level, effectively setting the upper limit of the noise floor. For simplicity, the noise floor is modeled as a constant level for $f > 15$ Hz. When an individual spectrum falls below the modeled noise floor, all higher frequencies are considered to have low signal-to-noise, and their spectral levels are set to zero. Thus T_z^2 variance is estimated using only the lower wavenumbers, where there is good signal-to-noise. Given the average fall rate of 6 cm s^{-1}, $f = 6$ Hz is equivalent to $k = 100$ cpm.

Fortunately, since most spectra exhibit exponential decay before falling into the noise floor, the present noise removal technique does not severely effect the results. Using the (minimum, average, maximum) spectra in Fig. A2, variance is estimated by subtracting the modeled noise floor, with a level set to match the spectrum at high frequencies. Probe response corrections are then made over all frequencies. The new χ estimates increase for the (minimum, average, maximum) spectra by (3%, 1%, 1%) respectively. Since $\langle \chi \rangle$ is determined by the large χ values, the pertinent corrections are for the average and maximum spectra. Therefore, the present technique of noise removal may lead to 1% underestimate of true $\langle \chi \rangle$.

The noise removal scheme also affects the probability distribution function of χ. Given the proximity of the distribution to lognormal (Fig. 10), it is important to clarify how much the noise correction influences the shape of the pdf. The data is reprocessed in two different ways. The modeled noise floor level is increased by 2, such that corrected spectra fall into this higher noise level sooner. Less of the spectrum is used to estimate χ, and so χ now have lower values. The second approach is to remove no noise at all. To avoid amplifying noise at high frequencies, no correction for probe time response is made. The results of these two approaches can be considered as error bounds on the cdf and imply that for $\chi < 3 \times 10^{-11}$ (where χ has low SNR) the cdf is significantly influenced by the noise correction scheme (Fig. A3).

The effect of the noise correction scheme has been further tested by modeling the input signal and noise. The temperature spectrum is modeled using the Batchelor spectrum for each realization. The level of χ (whose value is used to set ϵ and k_B) is given both a lognormal and cut-of-lognormal distribution (Davis 1994c). Added noise is modeled as a white spectrum, with a level matching observations at high frequencies (Fig. A2). The model's spectral shape is the Batchelor spectrum combined with the white-noise floor. The resultant χ is estimated in similar manners as above: No noise is removed; and when the combined spectrum approaches the noise floor, all higher wavenumbers are ignored (Fig. A4). When no noise is removed, the resultant cdf has no values with $\chi < 5 \times 10^{-11}$. However, the effect of the noise removal appears to have little impact on changing the true cdf at low χ. This is due to the exponential decay of the Batchelor spectrum: Noise will only have a significant effect on the spectrum when the peak spectral value and the noise floor are similar levels. This never occurs with the present model. The implication is that the observed low-valued χ spectra have a broader shape than the Batchelor spectrum, and thus at low SNR are more influenced on how the noise is subtracted.

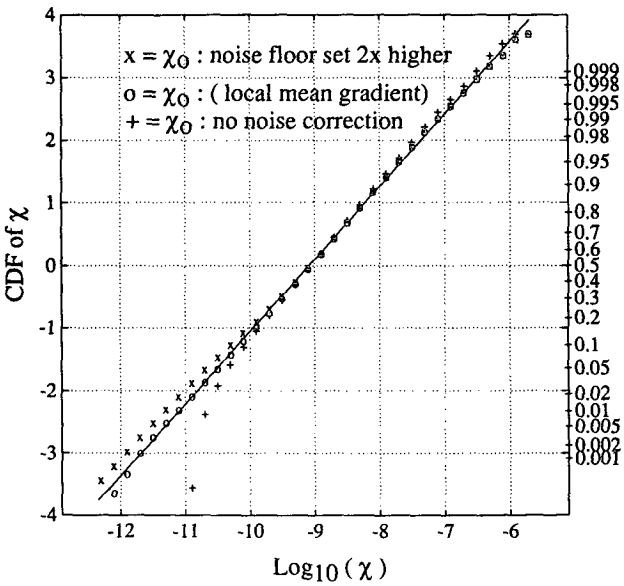

FIG. A3. The cdf of χ_0 is shown as computed in Fig. 10 (O), with removing no noise (+) and removing twice the original noise (×). Since removing no noise also does not attempt to do the probe response correction, high χ values (with large high-frequency variance) are biased low, resulting in its cdf being shifted to the left of the other two at large χ.

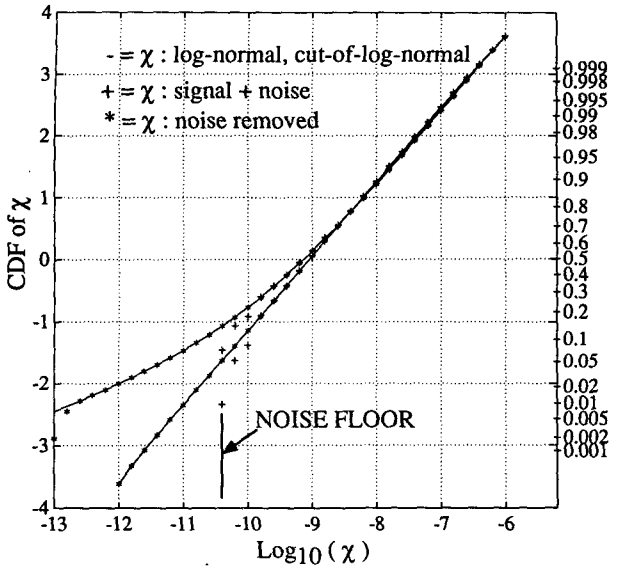

FIG. A4. Chi modeled as a Batchelor spectrum with added white noise. The variance in the Batchelor spectrum is modeled with both a lognormal (straight line) and cut-of-lognormal distribution (upper curve). The cdf is computed with no noise present (solid line), with noise present but not removed (+), and noise removed when the spectral level reaches the estimated noise floor (*).

It is of interest to explore other potential distributions of χ. Assume that there is 3D turbulence that exhibits a lognormal distribution and has the magnitude of its gradient, $G = |\nabla T|$. Davis (1994c) shows that any one component of the gradient (say T_z) is not lognormally distributed, but rather has a distribution he names cut-of-lognormal (Fig. A5).

Furthermore, since χ is estimated by averaging T_z^2 over some depth range Δz, the resultant χ is the average of N independent values of a cut-of-lognormal distribution. Therefore, the 0.5-m χ distribution should be neither lognormal nor cut-of-lognormal. Following Davis (1994c), cdfs are computed for $N = 1$, 2, 4, and 8 (Fig. A5). The values of the mean and variance of χ are allowed to vary such that the cdf at large χ matches the observed shape in Fig. 10. The measured distribution qualitatively matches well to either the lognormal distribution with $N = 1$ or the cut-of-lognormal distribution with $N = 2$–4. Due to averaging in depth, the ability to detect a cut-of-lognormal variable from a lognormal one is lost.

c. *Estimate of probe time response*

Probe response has been modeled as a double-pole filter with a -3 dB point at frequency f_c by Gregg and Meagher (1980) and Vachon and Lueck (1984). Both investigators found f_c to be dependent on fall rate U. Vachon and Lueck investigated the same type of thermistor as used on LAMP (Thermometrics FP07), such that their results are more relevant. They concluded that $f_c = 2.5U^{1/2}$ (units of U: cm s^{-1}, f: Hz), resulting in $f_c = 6.1$ Hz for the average LAMP fall rate of 6 cm s^{-1}. Individual probe response will depend upon the thickness of the glass coating during construction.

Lab tests have been conducted by dropping LAMP's probes through a temperature step and computing the resultant frequency response. Apparatus includes an 8-cm diameter vertical tube sealed with a thin rubber membrane at the lower end. The tube is filled with warm water and then partially lowered into a tank of cold water, thus forming the temperature step. Within 30 s after the membrane is in contact with the lower surface, the probe is dropped at the appropriate fall rate (6 cm s^{-1}). Small needles in front of, and to the side of the probe ($\sim$1 cm), break the membrane, and the probe samples the interface. This simplistic technique requires little setup time and cost overhead but produces marginal results due to variability in the interface, depending on how the membrane breaks. Of 50 profiles, only 12 displayed a relatively smooth, single-step interface, yielding 6 usable drops for each probe.

Probe response is compared with a theoretical step response that has thermally diffused across the membrane for the $\sim$30 s before the probe is dropped. Average frequency response for probe s/n 1 (Fig. A6) is similar to a double-pole filter with average $f_c = 8.3$ Hz, varying from 6.5 to 10.8 Hz for the 6 individual good drops. Wide variability of f_c indicates the unreliability

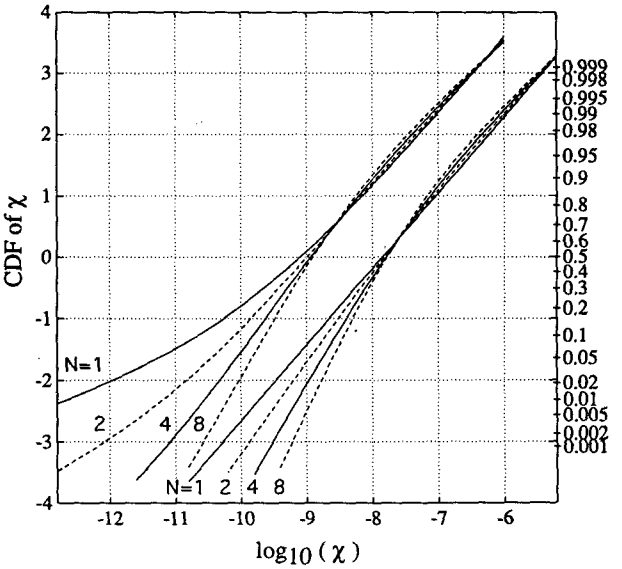

FIG. A5. The cdf of χ is shown assuming both a lognormal distribution (set of curves on the right) and a cut-of-lognormal distribution. The cdf is computed assuming that N independent values of χ are averaged over each 0.5 m measured estimate ($N = 1$, 2, 4, and 8, as marked). Mean and variance of each distribution is allowed to vary to produce the best fit for large χ, thus agreeing with the measured cdf of χ (Fig. 10). The distribution models are based on Davis (1994b).

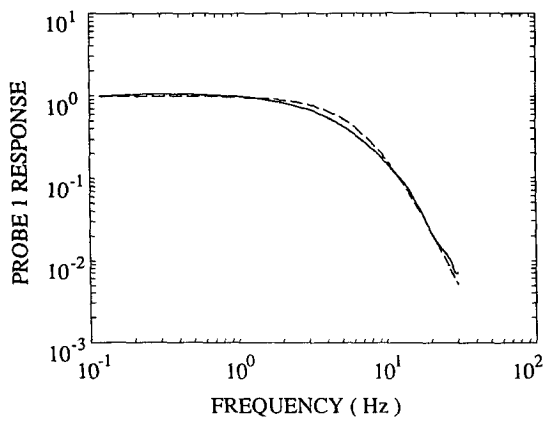

FIG. A6. Average frequency response for temperature probe s/n 1 (solid line) is compared with a double-pole filter with f_c = 8.3 Hz (dashed line). Results are from lab measurements of the probe to a step response.

of this technique. Deviation from a double-pole filter is most likely due to incorrectly modeling the true interface. Probe s/n 2 results are similar, with an average f_c = 9.2 Hz. Probes s/n 1 and 2 are the same sensors used on LAMP during the May 1992 deployment.

Resulting error in χ depends upon the individual spectral shape. Using the cruise-averaged spectrum in Fig. A2, varying f_c by (6.5/10.8) Hz causes χ to increase/decrease by (10/8)%. Likewise, using the maximum spectral level (Fig. A2), χ varies by 12%–16%. Since $\langle\chi\rangle$ is determined by the high-variance events, the latter numbers are more applicable. Based on the wide spread in χ from the lab measurements (which are inherently noisy due to the technique employed), $\langle\chi\rangle$ may vary by as much as ±15% due to incorrect modeling of the probe time response.

REFERENCES

Allredge, A. L., and M. W. Silver, 1988: Characteristics, dynamics and significance of marine snow. *Progress in Oceanography,* Vol. 20, Pergamon, 41–82.

Baker, M. A., and C. H. Gibson, 1987: Sampling turbulence in the stratified ocean: Statistical consequences of strong intermittency. *J. Phys. Oceanogr.*, **17,** 1817–1836.

Barham, E. G., 1979: Giant larvacean houses: Observations from deep submersibles. *Science,* **205,** 1129–1131.

Batchelor, G. K., 1959: Small-scale variation of convected quantities like temperature in turbulent fluid. *J. Fluid. Mech.*, **5,** 113–139.

Bendat, J. S., and A. G. Piersol, 1986: *Random Data: Analysis and Measurement Procedures.* Wiley-Interscience, 566 pp.

Davis, R. E., 1994a: Diapycnal mixing in the ocean: Equations for large-scale budgets. *J. Phys. Oceanogr.*, **24,** 777–800.

——, 1994b: Diapycnal mixing in the ocean: The Osborn–Cox model. *J. Phys. Oceanogr.*, **24,** 2560–2576.

——, 1994c: Sampling turbulent dissipation. *J. Phys. Oceanogr.*, submitted.

——, D. C. Webb, L. A. Regier, and J. Dufour, 1992: The Autonomous Lagrangian Circulation Explorer (ALACE). *J. Atmos. Oceanic Technol.*, **9,** 264–285.

Davoll, P. J., and M. W. Silver, 1986: Marine snow aggregates: Life history sequence and microbial community of abandoned larvacean houses from Monterey Bay, California. *Mar. Ecol.-Prog. Ser.*, **33,** 111–120.

Dillon, T. M., and D. R. Caldwell, 1980: The Batchelor spectrum and dissipation in the upper ocean. *J. Geophys. Res.*, **85,** 1910–1916.

——, 1982: Vertical overturns: A comparison of Thorpe and Ozmidov length scales. *J. Geophys. Res.*, **87,** 9601–9613.

Gargett, A. E., 1985: Evolution of scalar spectra with the decay of turbulence in a stratified fluid. *J. Fluid. Mech.*, **159,** 379–407.

——, and G. Holloway, 1984: Dissipation and diffusion by internal wave breaking. *J. Mar. Res.*, **42,** 15–27.

——, T. R. Osborn, and P. W. Nasmyth, 1984: Local isotropy and the decay of turbulence in a stratified fluid. *J. Fluid. Mech.*, **144,** 231–280.

Garrett, C., 1991: Marginal mixing theories. *Atmos.-Ocean,* **29,** 313–339.

Gregg, M. C., 1987: Diapycnal mixing in the thermocline: A review. *J. Geophys. Res.*, **92,** 5249–5286.

——, and T. B. Meagher, 1980: The dynamic response of glass-rod thermistors. *J. Geophys. Res.*, **85,** 2779–2786.

——, H. E. Seim, and D. B. Percival, 1993: Statistics of shear and turbulent dissipation profiles in random internal wave fields. *J. Phys. Oceanogr.*, **23,** 1777–1799.

Itsweire, E. C., J. R. Koseff, D. A. Briggs, and J. H. Ferziger, 1993: Turbulence in stratified shear flows: Implications for interpreting shear-induced mixing in the ocean. *J. Phys. Oceanogr.*, **23,** 1508–1522.

Ledwell, J. R., A. J. Watson, and C. S. Law, 1993: Evidence for slow mixing across the pycnocline from an open-ocean tracer-release experiment. *Nature,* **364,** 701–703.

McDougall, T. J., and Y. You, 1990: Implications of the nonlinear equation of state for upwelling in the ocean interior. *J. Geophys. Res.*, **95,** 13 263–13 276.

Munk, W. H., 1966: Abyssal Recipes. *Deep-Sea Res.*, **13,** 707–730.

——, 1981: Internal waves and small scale processes. *Evolution of Physical Oceanography,* B. Warren and C. Wunsch, Eds., The MIT Press, 264–291.

Osborn, T. R., 1980: Estimates of the local rate of vertical diffusion from dissipation measurements. *J. Phys. Oceanogr.*, **10,** 83–89.

——, and C. S. Cox, 1972: Oceanic fine structure. *Geophys. Fluid Dyn.*, **3,** 321–345.

——, and R. G. Lueck, 1984: Oceanic shear spectra from a submarine. *Internal Gravity Waves and Small-Scale Turbulence, Proc. Hawaiian Winter Workshop,* Honolulu, HI, Hawaii Institute of Geophysics, 25–50.

Rodriguez, J., and M. M. Mullin, 1986: Relation between biomass and body weight of plankton in a steady state oceanic ecosystem. *Limnol. Oceanogr.*, **31,** 361–370.

Schmitt, R. W., 1992: Preliminary Cruise Report: OCEANUS Cruise 250, leg 4, NATRE predeployment survey. Unpublished report, 30 pp.

Vachon, P., and R. G. Lueck, 1984: A small combined temperature-conductivity probe. *Proc. 1984 STD Conference and Workshop,* San Diego, CA, Mar. Technol. Soc., 126–131.